



## Remelt processing and microstructure of selective laser melted Ti25Ta

E.G. Brodie <sup>a, b, \*</sup>, A.E. Medvedev <sup>a, c</sup>, J.E. Frith <sup>a</sup>, M.S. Dargusch <sup>d</sup>, H.L. Fraser <sup>a, e</sup>, A. Molotnikov <sup>a, b, c, \*\*</sup>

<sup>a</sup> Department of Materials Science and Engineering, Monash University, Clayton, VIC, 3800, Australia

<sup>b</sup> Monash Centre for Additive Manufacturing (MCAM), 11 Normanby Road, Nottinghill, VIC, 3168, Australia

<sup>c</sup> RMIT Centre for Additive Manufacturing, RMIT University, Melbourne, Australia

<sup>d</sup> Centre for Advanced Materials Processing and Manufacturing (AMPAM), School of Mechanical and Mining Engineering, The University of Queensland, Brisbane, QLD, 4072, Australia

<sup>e</sup> Department of Materials Science and Engineering, The Ohio State University, Columbus, OH, 43210, USA



### ARTICLE INFO

#### Article history:

Received 2 August 2019

Received in revised form

15 November 2019

Accepted 18 November 2019

Available online 18 November 2019

#### Keywords:

Tantalum

Titanium

Selective laser melting

Biomedical

Mechanical properties

### ABSTRACT

In this study, elemental powder mixtures of Ti25Ta, an alloy with promise for orthopaedic applications, were processed using Selective Laser Melting (SLM), an emerging manufacturing method for bespoke implants. Material density and homogeneity was investigated as a function of laser scan speed and scanning strategy. Dense (>99.99%), pore free material was obtained at optimised processing parameters and a 'remelt' scan strategy improved melting of the Ta powders, avoiding keyhole formation.

Tensile and ultrasonic modulus testing of the SLM Ti25Ta revealed that the processed material had a similar yield strength to SLM commercially pure Ti, namely  $426 \pm 15$  MPa, with a significant reduction of elastic modulus to  $65 \pm 5$  GPa. The remelt scan strategy increased the yield strength to  $545 \pm 9$  MPa, without altering the elastic modulus, however reduced the elongation from  $25 \pm 1$  to  $11 \pm 4\%$ . TEM analysis revealed the microstructure consisted of predominantly hexagonal  $\alpha'$  martensite with a limited amount of orthorhombic  $\alpha''$  martensite formed in the Ta-rich regions near partially melted Ta particles, specifically facilitated by enhanced diffusion occurring during the remelt scan. The composition range for the  $\alpha''$  phase was observed to be approximately 40–50 wt% Ta. Electron back-scattered imaging (BSI) and back scattered diffraction (EBSD) revealed the formation of the prior  $\beta$  grains with close to equiaxed morphology and a slight texture in the  $\alpha'$  martensite. The application of the remelt scan disrupted the prior  $\beta$  grain structure and resulted in randomly oriented  $\alpha'$  laths.

Crown Copyright © 2019 Published by Elsevier B.V. All rights reserved.

## 1. Introduction

The biomedical implant industry is transitioning from conventional manufacturing of implants by machining, turning and milling to additive manufacturing [1]. Additive manufacturing (AM) enables the creation of complex parts from powders in a layer by layer fashion and can be used to produce patient specific implants. This transition opens up opportunities for developing new metallic alloys with improved mechanical, biological and wear properties. Among several AM techniques, powder bed fusion methods such as

selective laser melting (SLM) or electron beam melting (EBM) are preferred, as these methods can precisely control the geometrical features of the implants.

Commonly used metallic implants are produced from stainless steel, cobalt based or titanium based alloys. Among these materials, titanium based alloys are favoured due to their biocompatibility, corrosion resistance, light weight and fatigue strength [2]. However, existing titanium alloys, such as Ti–6Al–4V, have a high elastic modulus (~110 GPa), which leads to bone resorption by stress-shielding [3]. Several studies have also reported toxicity concerns regarding the use of Al and V in the body [4–6]. Therefore, new  $\beta$ -type titanium alloys, such as Ti–24Nb–4Zr–8Sn (TNZS) and the Ti–Ta system are emerging, promising a much lower elastic modulus. However, these alloys often contain high melting temperature constituents, such as niobium and tantalum, which complicate their processing.

Alloys which contain refractory components, are conventionally

\* Corresponding author. Department of Materials Science and Engineering, Monash University, Clayton, VIC, 3800, Australia.

\*\* Corresponding author. RMIT Centre for Additive Manufacturing, RMIT University, Melbourne, Australia

E-mail addresses: [erin.brodie@monash.edu](mailto:erin.brodie@monash.edu) (E.G. Brodie), [andrey.molotnikov@rmit.edu.au](mailto:andrey.molotnikov@rmit.edu.au) (A. Molotnikov).

arc melted several times to achieve a homogeneous solid solution [7–11]. The solidified material is then difficult to machine into complex shapes, due to its high strength and hardness. Selective laser melting provides an alternative route for processing of these alloys which facilitates blending and melting of different constituents, while simultaneously fabricating complex geometries with intricate features, such as scaffolds.

New developed alloy systems successfully produced by SLM, such as  $\beta$ -Ti–Nb–Zr (TNZ) and  $\beta$ -Ti–Nb–Zr–Sn (TNZS) [12–15], possess a lower elastic modulus and demonstrate favourable mechanical properties. For instance, Li et al. [13] reported the fabrication of  $\beta$ -Ti–35Zr–28Nb solid and lattice structures using the SLM process. The SLM produced solid samples possessed an elastic modulus in the range of 57–60 GPa. A lower elastic modulus of 42–55 GPa was reached by Zhang et al. [14], by the addition of Sn, and an acetabular cup was successfully manufactured. However, difficulties in the laser processing of multi-constituent alloys was highlighted, as the evaporation of the lower melting point element Sn led to pore formation [16]. Binary alloy systems, such as Ti–Nb, have also been investigated via SLM [17–19]. Despite displaying a higher elastic modulus of 61–77 GPa [17,20], the alloys with higher concentrations of particular elements, such as Nb and Ta, may offer a biological advantage [18,21,22].

Another promising alloy system for biomedical applications is the Ti–Ta system. Tantalum acts as a  $\beta$ -phase stabiliser in titanium, influencing the elastic and tensile properties depending upon composition. Furthermore, Ta is reported to have a positive effect on bone formation [23–27]. Zhou et al. [7,28] studied the variation of Ta content for conventionally fabricated samples and concluded that the Ti25Ta composition possessed the highest strength-to-modulus ratio from the Ti–Ta system. The broader adaptation of this alloy system is hindered by the cost of tantalum and the difficulty of its processing.

Several studies have begun to investigate the feasibility of SLM processing of pure tantalum and the Ti–Ta alloy system [26,29–33]. For instance, Wauthle et al. [26] first produced bulk and porous structures using pure tantalum. They concluded that tantalum had superior osteoconductive properties compared with Ti–6Al–4V and higher normalised fatigue strength. However, a strong anisotropic structure was noted and has been observed again in more recent studies [30]. Material failure is often due to regions where full powder melting has not occurred [29]. Sing et al. [31,32] used selective laser melting to successfully produce a Ti50Ta alloy by mixing elemental Ti and Ta powders. It was shown that the obtained alloy had a  $\beta$ -phase microstructure with an elastic modulus of  $75.77 \pm 4.04$  GPa and a good combination of strength and ductility (UTS of 924 MPa and elongation of 11%). It was also identified that the full melting of Ta particles was challenging, as unmelted Ta particles remained in the matrix. The persistence of unmelted Ta particles after SLM processing has since been confirmed in other compositions ranging from 6 wt% - 25 wt% Ta [33].

The difficulty of processing alloys with refractory components, such as Ti25Ta, lies in the ability to simultaneously hold two materials, with very different melting points, in the molten state. Several studies discuss the feasibility of SLM processing of alloys which comprise of elements with different melting characteristics and show preferential vaporisation of the lower melting point constituents [16,34,35]. SLM processing uses a laser to melt and densify a powder layer and the most common processing parameters include: laser power ( $P$ ), scan speed ( $v$ ), hatch distance ( $h$ ) and layer thickness ( $t$ ). These parameters must be carefully controlled to obtain a processing window for any new alloy composition, in order to produce homogeneous and defect free material. One widely used method to characterise the process is to use the volumetric energy

density equation, Equation (1), which combines the critical processing parameters into a single variable, [36–39].

$$E = \frac{P}{vht} \quad (1)$$

However, Equation (1) does not take into account chemical composition, thermal conductivity and diffusivity of the constituents and is therefore known to have a limited predictive capability. An alternative methodology was proposed by King et al. [40]. They suggested that the processing window can be related to a ‘specific enthalpy’  $\Delta H/h_s$ , see Equation (2).

$$\frac{\Delta H}{h_s} = \frac{AP}{h_s \sqrt{\pi D v \varnothing^3}} \quad (2)$$

Here,  $A$ ,  $D$ ,  $T_m$ ,  $\kappa$ ,  $\varnothing$  represent absorptivity, thermal diffusivity, melting temperature, thermal conductivity and specific laser spot size, respectively and  $h_s$  is given by Equation (3).

$$h_s = \frac{T_m \kappa}{D} \quad (3)$$

The specific enthalpy model predicts a region of defect formation, known as keyhole formation, at specific enthalpy values of approximately  $30 \pm 4$ . There has been no investigation in to whether Equation (2) can provide a good indication of the processing parameters required to create a homogeneous solid solution from a mixed powder alloy, such as Ti25Ta.

SLM produced materials from mixed powders must be assessed for chemical homogeneity, as well as porosity. Studies exploring mixed powders highlight the inhomogeneity in the as-built material [33,41–44], however little is understood concerning how partially melted particles affect the deformation mechanisms and failure of the material. Post-heat treatment is often recommended to fully incorporate partially melted particles [43], however increasing the alloy homogeneity during part building saves processing time and cost. Pre-alloyed powders provide one solution to increasing homogeneity [20,45,46], but limit alloy flexibility and are not currently widely available, particularly for refractory metals which require plasma atomisation.

Several studies have reported the application of a ‘remelt’ scan strategy to successfully increase the density and improve the surface finish of SLM produced parts, particularly when applied to refractory materials such as tungsten [47–53]. A second laser pass per layer, provides a second melting opportunity for powder particles and preliminary studies show that this can increase the homogeneity of alloys with refractory constituents such as Nb [54], as well as be used to tailor the microstructure [48,55,56]. It is yet to be shown whether this strategy is suitable for the Ti–Ta system, where the constituents possess an even larger difference in melting temperature. This technique could prove critical in the laser processing of this hard-to-manufacture alloy system. In addition, the effects of the remelt scan on the microstructure and mechanical properties of SLM produced material have not been investigated in depth.

In this study, Ti25Ta was selected as a promising biomedical Ti alloy. We report the successful production of bulk material via SLM from mixed powders. The processing parameters were investigated and compared with the specific enthalpy model to determine optimal printing parameters. In addition, a remelt scan strategy was explored as an approach to improve material homogeneity and minimise the volume fraction of partially melted Ta particles. Tensile samples and samples for ultrasonic modulus testing were manufactured and the mechanical properties compared with

SLMed commercially pure (CP) Ti and the TNZS alloy. Finally, the effect of the remelt scan strategy on the microstructure formation and morphology is discussed.

## 2. Material and methods

### 2.1. Powder morphology and preparation

Commercially pure titanium (Grade 1 ASTM B861, TLS Technik Spezialpulver, Germany) and tantalum (TEKNA, Canada) powders were combined in a 3:1 wt ratio and tumble mixed for 12 h at 15 rpm. Both powders were spherical in shape, Fig. 1, and were of a similar size distribution (Ti: 20–45 µm and Ta: 15–45 µm) to ensure dense packing on the powder bed and high final part density. The chemical compositions of the powders are displayed in Table 1, highlighting the pre-manufacturing oxygen concentration.

### 2.2. Selective laser melting of Ti25Ta

Samples for density optimisation and mechanical testing were prepared using a Concept Laser Mlab Cusing machine with a 100 W Nd:YAG 1070 nm wavelength laser and a 50 µm spot size (Concept Laser GmbH, Germany). Printing was conducted under an argon atmosphere with the oxygen content below 0.2%. A scanning strategy, consisting of a single continuous laser path running at 45° to the y-axis and running back in the opposite direction once reaching the edge of the part, was applied. A 90° rotation of this scanning pattern was applied between layers.

The laser power was held at the machine maximum (95 W), due to the expected high energy input required to melt the Ta particles. The scan speed was varied between 100 and 700 mm/s to investigate the effect of specific enthalpy on material formation. The hatch distance and layer thickness were kept constant at 35 µm and 25 µm, respectively. In addition, a remelt scan was applied to half of the samples to investigate the effect on homogeneity. The remelt scan consisted of the same parameters and scan path as the first laser scan.

Square samples (15 mm × 15 mm × 10 mm) were printed and assessed optically for porosity and remaining partially melted Ta particle area. Optimised parameters were chosen from these results and were used to print tensile blocks (20 mm × 15 mm × 70 mm) and further square samples for ultrasonic modulus testing. The tensile samples were machined from the printed block using electrical discharge machining (EDM). The tensile sample size was designed in accordance with ASTM standard E8 to fit within the

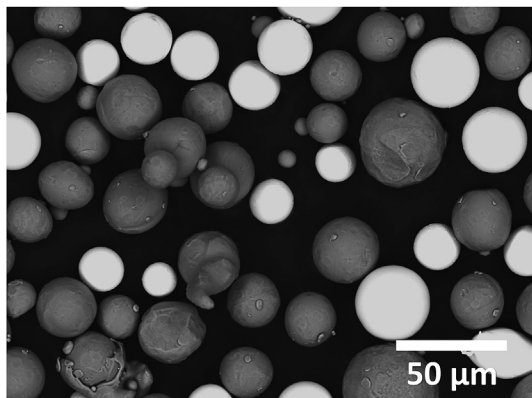


**Fig. 1.** Back-scattered image of mixed Ti25Ta powders showing spherical Ti and Ta particles. Ta powder particles appear light grey/white due to their higher density compared with the Ti powders which are seen as dark particles.

**Table 1**

Chemical composition of as-received powders, as measured by suppliers.

	Ta	Ti	O	Fe	N	C
Ta	>99.95%	—	0.033	≤0.001	≤0.001	≤0.001
Ti	—	Bal.	0.11	0.012	0.009	0.006

build volume of the Mlab Cusing.

### 2.3. Microstructure characterisation, homogeneity analysis and oxygen content investigation

The square samples were cross-sectioned in the y-z plane to assess porosity and homogeneity. The samples were mechanically ground and polished using 0.04 µm OP-S colloidal silica solution. No etching was conducted.

Optical images were taken with a GX51 Optical Microscope at 10× magnification. ImageJ analysis software was used to measure the image area percentage of porosity and partially melted Ta particles for each sample using thresholding techniques. Area fraction values were calculated as an average from five images, spread over the sample cross-sectional area.

Samples were ion beam polished at 300 µA and 7 kV for 10 min followed by 100 µA and 3 kV for 15 min for scanning electron microscopy (SEM) analysis and a JEOL 7001F FEG SEM was used. Back scattered images (BSI) were also taken to assess the distribution of tantalum throughout the material and analysis was supported by electron dispersive X-ray spectroscopy (EDS) measurements. Microstructure morphology and texture was assessed using electron back scattered diffraction (EBSD) imaging to create inverse pole figure (IPF) maps.

The samples were tested for chemical composition using elemental spectroscopy (Spectrometer Services Pty Ltd) to identify oxygen content and to support microstructure analysis. X-ray diffraction (XRD) was used to identify the crystallographic phases present in the printed samples. A Bruker D8 Advance X-ray diffractometer with a Cu Kα X-ray source was used and scans from 30 to 100° conducted, at 0.02 increments at a speed of 1 s per step.

The TEM foils were prepared using a focused ion beam (FIB) milling and lift-out technique, performed with an FEI Scios Dual-beam FEGSEM. FIB lamellas were prepared for both single melt and remelt conditions in regions with Ta-nominal and Ta-rich concentrations. The microstructure was then observed with a JEOL 2100F FEGTEM equipped with an Oxford X-MaxN EDX detector at an accelerating voltage of 200 kV. Bright field imaging, selected area electron diffraction (SAED) and EDX analysis were carried out to determine the morphology and chemical composition of the constituent phases.

### 2.4. Mechanical characterisation

Uniaxial tensile testing was conducted with a 4505 Instron tensile machine, equipped with a 100 kN load cell and an extensometer. Specimens were tested in the build direction (z-axis), at a strain rate of 0.2 mm/min, until fracture. A minimum of five samples were tested for each condition for reproducibility. Fractography analysis was undertaken of the fracture surfaces using a JEOL 7001F FEG SEM in back-scatter imaging (BSI) mode.

The elastic modulus of the printed material was measured using ultrasonic modulus testing. A parallel faced sample was prepared and its density and thickness measured. The sonic velocity of longitudinal and transverse waves was measured using an Olympus 702 PR pulse processor and a Fluke 190–204 Scopemeter. These measurements were used to calculate the Poisson's ratio, and

elastic modulus as in Refs. [17,57]. A dynamic method was chosen in this work as it provides a more accurate measurement of the elastic modulus than the results obtained from tensile testing [58].

### 3. Results and discussion

#### 3.1. Selective laser melting processability of TiTa alloy

Square samples were printed over a range of scan speeds resulting in all samples with density above (>99.7%), Fig. 2a. It can be seen that the optimal scan speeds lay between 300 and 500 mm/s and dense (>99.99%) and pore free material was obtained, Fig. 2b. These parameters and Equation (1) give a higher energy density (217–362 J/mm<sup>3</sup>) than the optimal parameters identified by Sing et al. [31] for Ti50Ta (144 J/mm<sup>3</sup>). The higher weight percent of tantalum in the Ti50Ta composition would intuitively require a larger energy density, and hence the limitations of this optimisation variable are shown.

It was observed that at higher scan speeds the porosity increased due to a lack of fusion, while at lower scan speeds keyhole formation was detected, where excessive energy density causes vaporisation. The resulting vapour pressure forms a deep depression in the melt pool where an imbalance with the liquid metal surface tension leads to collapse of the depression and pore formation in the melt pool wake [40,59,60]. As this type of pore is formed due to vapour pressure at the bottom of the conical melt pool, the pore morphology ranges from spherical to conical. Pores taking the conical shape at the bottom of the melt pool, as shown in Fig. 2c, are indicative of SLM processing [16,36,61] and were also noted in our preliminary single scan investigations (shown in Supplementary Fig. 1). A small increase in porosity above and below the optimal parameter range is consistent with published results in other parameter optimisation studies [34,59,62].

The remelt scan strategy had no effect on the density in the optimal scan speed range, between 300 and 500 mm/s, but led to an increase in density above the optimal parameter zone and decreased the density below the optimal parameter zone. This may support our observation that excessive input energy causes the increase in porosity, as a second melting scan has compounded the volume of pores. However, the sample produced at 200 mm/s deviated from the overall trend and showed a higher porosity than

the sample produced at 100 mm/s, suggesting an additional mechanism of pore formation. Multiple studies investigating spatter particle formation and flying trajectory have found that the vapour plume created by the laser causes spatter particles, travelling at 400–900 mm/s, to pass through the incident laser beam [63–66]. It is hypothesised that these spatter particles lead to an increase in defect formation by their high oxygen content, which reduces subsequent particle wetting, or through the formation of larger spatter agglomerations, which do not fully melt. It is possible that at such low scan speeds of 100–200 mm/s, the interaction time of spatter with the incident laser beam is increased, contributing to the increase in porosity noted at 100–200 mm/s. However, this hypothesis does not explain why the porosity should be greater at 200 mm/s than 100 mm/s, as the laser-spatter interaction time would be decreased at 200 mm/s. Further studies, such as an exploration of the interaction between the speed of the spatter particles and the speed of the laser, are required to assess laser-spatter interactions at low scan speeds and to explain the observed porosity increase at 200 mm/s.

Fig. 2b and c shows remaining Ta particles which have not been fully melted and incorporated into the matrix. As mentioned in the introduction, full melting of refractory materials such as Ta particles is very challenging. Back scattered images of the sample y-z plane were collected for the range of speeds between 100 and 700 mm/s to evaluate the area fraction of partially melted Ta particles, Fig. 3a. The chemical nature of the particles was confirmed using EDS analysis. It was found that the area fraction of partially melted Ta particles decreased with decreasing scan speed. Furthermore, the remelt scan strategy was successful at reducing the area percent of partially melted particles, by up to 60%, Fig. 3a. Overall, the area percentage of partially melted Ta particles plateaus at ~0.25%.

Both density and homogeneity must be assessed simultaneously to determine the optimal printing parameters for SLM processing of mixed powder alloys, such as Ti25Ta. A high energy input is required to successfully melt refractory constituents, such as tantalum, however excessive energy inputs can cause vaporisation and keyhole formation, as demonstrated in Fig. 2c. While basic parameter studies focus on achieving a fully dense part utilising the volumetric energy density equation, Equation (1), this approach lacks the ability to address the issue of homogeneity.

One alternative method is to use a specific enthalpy  $\frac{dH}{ds}$  measure,

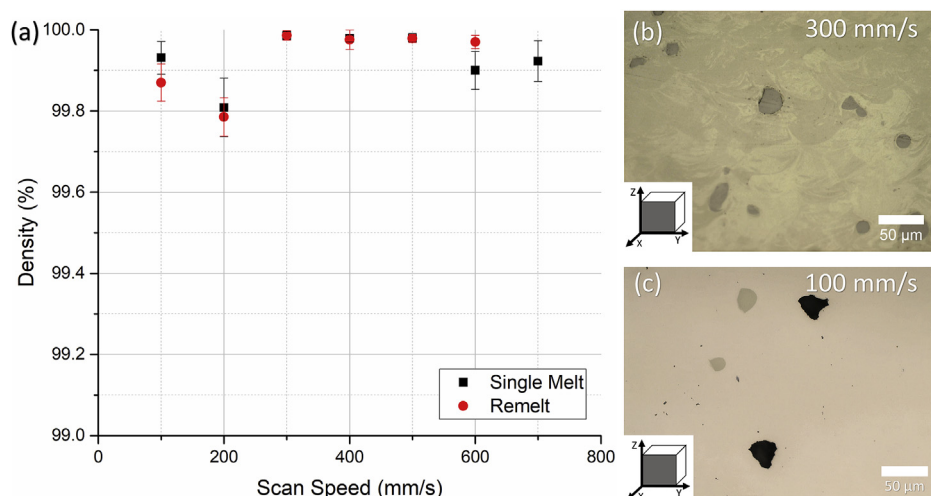


**Fig. 2.** (a) Density of Ti25Ta parts for different scan speeds and application of two different melting strategies, namely single melt or remelt scan. (b) Optical micrograph of a cross-section of a Ti25Ta part obtained at the velocity of 300 mm/s showing a fully dense part with a small fraction of remaining partially melted Ta particles and (c) a Ti25Ta part obtained at the velocity of 100 mm/s displaying conical shaped pores typical of keyhole formation.

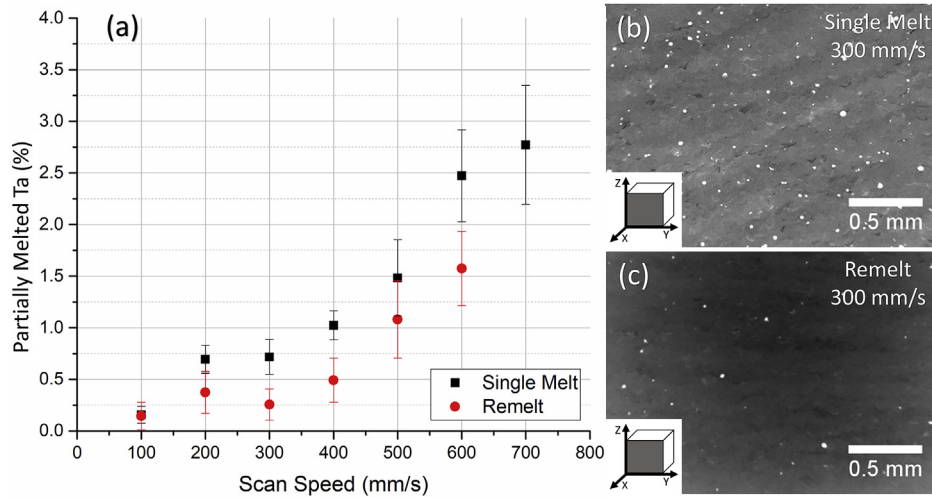


**Fig. 3.** (a) Area percentage of partially melted Ta particles for different scan speeds and melting strategies. (b) Back scattered image of a cross-section of a Ti25Ta part highlighting the partially melted Ta particles within the single melt scan sample obtained at 300 mm/s velocity and (c) its counterpart after application of the remelt scanning strategy showing the reduction in partially melted Ta particles within the Ti25Ta part.

Equation (2), as proposed by King et al. [40] which uses parameters that are directly linked to the chemical nature of the powder. The material constants used in the model are summarised in Table 2. Here, the thermal diffusivity, thermal conductivity and absorptivity of the Ti25Ta composition were estimated from the atomic composition and the melting temperature was taken from thermodynamic calculations obtained using ThermoCalc software. Literature reports the absorptivity of titanium powder between 0.65 and 0.77 [67,68]. Hence, the average value 0.71 was used and an error of  $\pm 0.05$  applied. As no value for the absorption of tantalum powders could be found in literature, we used the information about the extinction co-efficient ( $k$ ) to estimate absorptivity values. It was reported that the extinction co-efficient ( $k$ ) for Ta obtained at 1070 nm wavelength absorbs more strongly than Ti ( $k = 5.39$  to  $k = 3.34$ ) [69]. Therefore, the absorptivity of Ta powder is taken to be slightly higher than that of Ti, 0.75.

The suitability of this model to predict optimal printing parameters for the Ti25Ta mixed powder composition is assessed by plotting the predicted values for Ti25Ta and comparing them to the experimentally obtained porosity values, Fig. 4. The models for pure Ti and pure Ta are plotted for comparison.

The curves for pure Ti and pure Ta in Fig. 4 highlight the different melting characteristics of the two materials. Ta is difficult to process via SLM not only due to its high melting temperature, but also its high thermal conductivity. As Ta transfers heat to its surroundings quickly, Ta powder particles will have higher cooling rates than Ti powder particles, resulting in less time for melting and mixing within the melt pool.

The model indicates that the onset of keyhole melting is

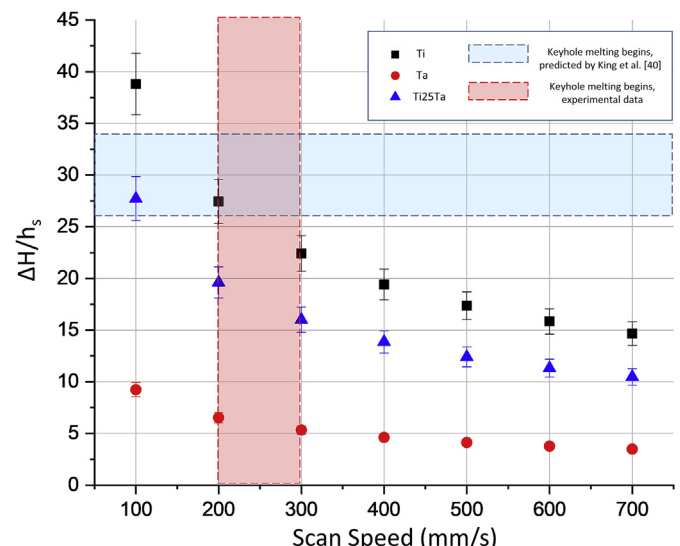


**Fig. 4.** Numerical model predicts vaporisation in pure Ti and the Ti25Ta alloy at scan speeds below 300 mm/s and 200 mm/s respectively. The blue horizontal region displays the specific enthalpy at which keyhole formation begins, predicted by King et al. [40]. The samples printed in this study showed pore formation beginning at 200–300 mm/s scan speeds, shown by the red vertical region. The numerical method is more appropriate for pre-alloyed powders, as for mixed powders the laser beam size and particle size are too similar, resulting in single particle laser interactions with distinct elements. The error value was included due to the estimation used for powder absorptivity. (For interpretation of the references to colour in this figure legend, the reader is referred to the Web version of this article.)

**Table 2**

Physical properties of Ti and Ta powders used in calculations. Due to lack of experimental data in literature, starred values are calculated as follows: \*Using atomic percentage of alloy and pure Ti/Ta values \*\*Using ThermoCalc database \*\*\*Estimated from absorptivity data which shows Ta absorbing higher than Ti [70,71].

	Ti	Ta	Ti25Ta
Thermal Conductivity (W/mK)	21.9 [72]	57.5 [72]	24.7 *
Melting Temperature (K)	1387 [72]	3027 [72]	1771 **
Thermal Diffusivity (cm <sup>2</sup> /s)	0.120 [73]	0.200 [74]	0.126 *
Absorptivity	0.71 [67,68]	0.75 ***	0.71 *

expected at scan speeds between 200 and 300 mm/s for pure titanium, but between 100 and 200 mm/s for the Ti25Ta alloy. However, the experimental data shows an onset of porosity, deduced as likely keyhole pores from the pore shape and the high energy density parameters, between scan speeds of 200–300 mm/s for the SLM Ti25Ta. This suggests that the processing of mixed powder Ti25Ta is limited by the processing capabilities of the lower melting temperature element, Ti. The higher energy density, required to melt the refractory constituent, is not evenly dispersed throughout the powder as the spot size of the laser (50  $\mu\text{m}$ ) is very similar to the powder particle size (15–45  $\mu\text{m}$ ) [68]. This results in

moments when the laser is focused on only one particle of the Ti, causing excessive energy input and keyhole formation. The contact with refractory powder particles with high thermal conductivities, is not sufficient to draw heat away from the melting particles and avoid vaporisation and melt pool instabilities.

The proposed model has several limitations. For instance, it fails to accurately represent mixed powder alloys as it does not consider the thermal interactions between powder particles of a different chemical nature. Direct measurements of the thermal diffusivity, thermal conductivity and absorptivity could remove the need for the approximation by the rule of mixtures and could improve the predictive capabilities of the model. Despite these shortcomings, the model allows us to draw important conclusions. It highlights that altering the energy density via scan speed is not sufficient to create high density, homogeneous material from mixed powder Ti25Ta. Increasing the energy density causes keyhole formation in the Ti before full Ta melting can be achieved. Hence, other approaches, such as altering the scan strategy, are essential to process refractory mixed powder alloys.

The remelt scan strategy was successful at reducing the remaining volume of partially melted Ta particles. The increase in homogeneity caused by the remelt scan is likely due to the second opportunity for physical mixing in the molten state, as opposed to the energy density used for the scan. These aspects will be further discussed in section 4.

It can be concluded that the application of a single remelt scan was able to reduce the remaining partially melted Ta volume to below  $\sim 0.25\%$ . It is likely that the application of successive remelt scans would further reduce this number. However, the effect of the remelt scan on the mechanical properties and the resulting microstructure must first be understood.

### 3.2. Mechanical properties

The SLM as-built Ti25Ta samples were tested under uniaxial tension to determine the mechanical properties for both the single scan and remelt scan strategies. The single scan and remelt scan samples showed an ultimate tensile strength of  $509 \pm 7$  MPa and  $566 \pm 6$  MPa respectively, with corresponding total elongations of  $25 \pm 1\%$  and  $11 \pm 4\%$ , Fig. 5. Both samples show a softening deformation behaviour during elongation. This behaviour is commonly

seen in pure titanium and is attributed to a high rate of dislocation annihilation, due to a lower activation energy for self-diffusion in alpha titanium, than the activation energy for deformation [75–78].

Both the single melt and remelt samples show an increase in ultimate tensile strength compared with conventionally wrought grade 1 CP Ti (240–331 MPa [79]) and comparable values to conventionally produced Ti25Ta (560 MPa [7]). Typically, SLM processed materials are stronger than conventionally wrought material due to a finer grain structure and increase in dislocation density [80]. However, conventionally wrought and quenched Ti25Ta already typically forms heavily dislocated fine lath structures [9,10,28,81].

Another important factor which affects the mechanical properties of titanium alloys is the oxygen content. In pure titanium oxygen acts as a strengthening agent and can raise the ultimate tensile strength to 660 MPa with 0.4 wt% additions [79]. Therefore, we conducted elemental spectroscopy to determine the uptake of oxygen during the SLM process for both scanning strategies. It was found that SLM processed Ti25Ta contained  $0.13 \pm 0.03$  wt% oxygen, hence still falling within the class of ASTM grade 1 titanium [81]. The oxygen content of the remelt scan sample increased by 0.04 wt % compared with the single scan sample. This small rise in oxygen content is insufficient to provide the entire 50 MPa of additional strength observed in the remelt scan sample, highlighting that the main contribution to the increase in strength is associated with microstructural changes. The microstructural changes induced by the remelt scan also cause a decrease in the elongation, which will be further discussed in section 4.

The single melt sample shows a similar elongation to both conventionally produced grade 1 Ti (30% [79]) and conventionally produced Ti25Ta (20–22% [7]). High ductility is common in SLM produced Ti and is linked to the grain refinement from high cooling rates [80]. The high ductility of the single melt scan sample supports that the remaining partially melted Ta particles in the samples are not compromising their mechanical behaviour. This was further investigated via fracture analysis of the tensile samples.

SEI and BSI images showed very similar fracture surfaces between the single melt and remelt scan samples. The single melt sample fracture surface showed more partially melted Ta particles, as highlighted in Fig. 3, however this appeared to have no effect on the morphology of the fracture surface. Hence, only the remelt scan fracture surface is displayed in Fig. 6a and b, which highlight the ductile and brittle fracture regions observed. The ductile region was focused in the centre of each sample and characterised by dimple morphology, suggesting failure was initiated at internal pores. The surface area of the ductile region was slightly larger for the single melt scan sample, which corresponds with its larger elongation. BSI confirms that the remaining partially melted Ta particles do not correspond to the dimple shape or distribution and hence, are unlikely assisting cavity formation or failure. This highlights that the material density is more critical to mechanical performance than the remaining partially melted Ta fraction.

The elastic region of the tensile curves suggested elastic modulus values of  $35 \pm 8$  GPa and  $47 \pm 3$  GPa for the single melt and remelt scan samples respectively. However, dynamic methods of modulus measurement are recognised as more accurate [58] and ultrasonic testing produced modulus values of  $65 \pm 5$  GPa for both the single melt and remelt scan samples. This value is more closely in agreement with literature (64 GPa [7]). A significant reduction of modulus compared with pure titanium (103 GPa [79]) is observed, caused by the increase of titanium lattice size due to Ta atom substitutions [7].

The increase in strength and decrease in modulus of the Ti25Ta alloy compared with CP Ti is promising for biomedical applications,

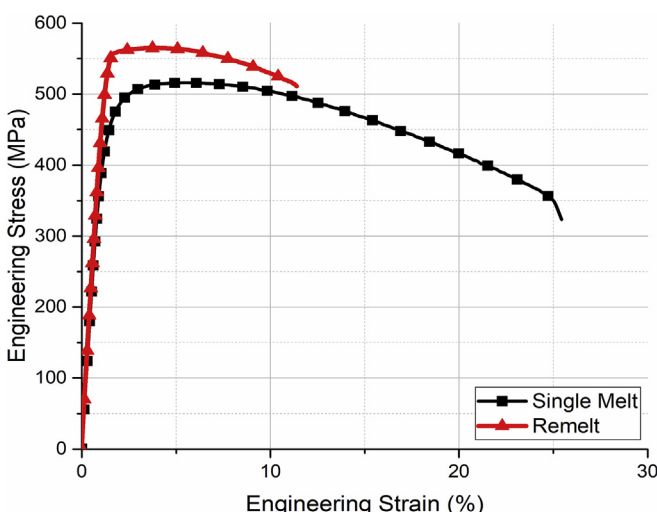
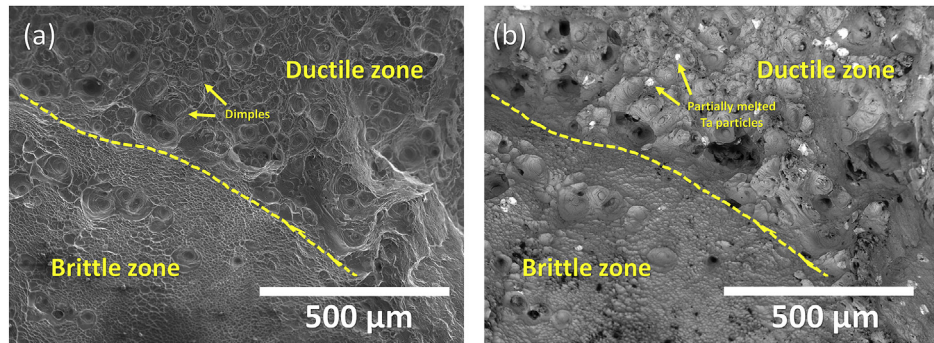


Fig. 5. Engineering stress-strain curves of single and remelt scan Ti25Ta samples produced by SLM. The remelt scan strategy causes an increase in strength, while preserving some elongation.



**Fig. 6.** Fractography of failed Ti25Ta remelt scan tensile sample showing the boundary of brittle to ductile zones. (a) Secondary electron image (b) back scattered electron image. Ductile zones show dimpled regions and cavity formation. Partially melted Ta, which appears bright in the image, is homogeneously dispersed in the fracture region.

as a balance of these properties is critical in reducing stress shielding in orthopaedic implants [82]. It should be emphasised that these mechanical properties are preserved after SLM processing, making SLM an attractive manufacturing method of bespoke medical implants. Table 3 summarises the comparison of this work's results to conventionally produced Ti25Ta, pure titanium and the TNZS alloy. The yield strength to modulus ratio is often considered an adequate measure for comparing different materials for biomedical applications. The SLM produced Ti25Ta has a superior yield strength to modulus ratio compared with both the SLM and conventionally produced CP Ti.

The SLM Ti25Ta alloy is still inferior in strength to modulus ratio to the TNZ, Ti50Ta and TNZS alloys. However, its superior ductility and biomedical benefits may make it more applicable to orthopaedic applications. In particular, the higher ductility is likely to lead to a superior fatigue strength, a critical quality for many orthopaedic implants [85]. Further work on developing an appropriate heat treatment and an investigation of the fatigue performance is underway and will be reported elsewhere.

### 3.3. XRD phase analysis

The phase structure of the Ti and Ta powders, as well as the SLM Ti25Ta, was observed using XRD techniques. The Ti powder possessed a HCP structure whilst the Ta powder showed a BCC structure, confirmed with PDF cards 00-044-1294 and 00-004-0788 respectively, Fig. 7. The SLM Ti25Ta showed alpha peaks. The alpha peaks of the SLM Ti25Ta have been labelled as  $\alpha'$  in Fig. 7, as this is the martensitic non-equilibrium form of the equilibrium stable  $\alpha$  phase, with the same crystal structure.

The XRD peak data of the SLM Ti25Ta is shifted slightly to the left of that of the Ti powder. This shift indicates an increase in atomic

lattice size as Ta atoms fill substitutional lattice positions and agrees well with the observed drop in elastic modulus. In addition, peak broadening is observed which suggests residual strain in the material, a common result from the rapid solidification of SLM processing [86].

### 3.4. Microstructural analysis

The XRD analysis only indicated the presence of hexagonal martensite  $\alpha'$  in the structure of all samples. However, it has been reported that Ta concentrations of 25 wt% or more may lead to the formation of orthorhombic martensite ( $\alpha''$ ) [7]. Here, the results from further microstructural analysis using TEM are presented. This analysis was undertaken to investigate the presence of  $\alpha''$  which was not identified by XRD.

The results in Section 3.1 and Fig. 3 indicate that some partially melted Ta particles were present in the bulk specimen even after a remelt scan strategy was applied. It should be noted that due to the inhomogeneity of the material, TEM analysis is limited in its representation of the bulk microstructure. However, as a small volume of partially melted Ta particles remain in the material, we are presented with a unique opportunity to investigate the changing crystal structure over a range of wt% Ta compositions. Regions surrounding partially melted Ta particles are of particular interest as the increased concentration of Ta makes the formation of  $\alpha''$  martensite more feasible and the transition between the  $\alpha'$  and  $\alpha''$  phases can be investigated. Therefore, both single scan and remelt scan samples have been analysed and regions with nominal Ta composition as well as a region in the vicinity of a partially melted Ta particle have been analysed to achieve a representative investigation.

Fig. 8 shows the microstructure of nominal composition regions

**Table 3**  
Comparison of mechanical properties of SLM and conventionally produced biomedical alloys.

	Total Elongation (%)	Yield Strength (MPa)	Elastic Modulus (GPa)	Yield strength: Modulus	Reference
SLM					
Ti25Ta Single Melt	25 ± 1	426 ± 14	65 ± 5	6.6	This work
Ti25Ta Remelt	11 ± 4	545 ± 9	65 ± 5	8.4	This work
CP Ti	19.5 ± 1.8	555 ± 3	112 ± 3 [31]	5.5	[62]
Ti–24Nb–4Zr–8Sn (TNZS)	19 ± 4	563 ± 38	53 ± 1	10.6	[34]
Ti50Ta	12 ± 1	883 ± 20	76 ± 4	11.6	[31]
Ti–35Zr–28Nb (TNZ)	–	612 ± 29	57 ± 2	10.7	[13]
Conventional					
Ti25Ta	20	480	64	7.5	[28]
CP Ti	30	170–241	103	2.0	[79]
Ti–24Nb–4Zr–8Sn (TNZS)	15	700	46	15.2	[83]
Ti50Ta	25	375	77	4.9	[7]
Ti–35Zr–28Nb (TNZ)	11	729	64	11.4	[84]

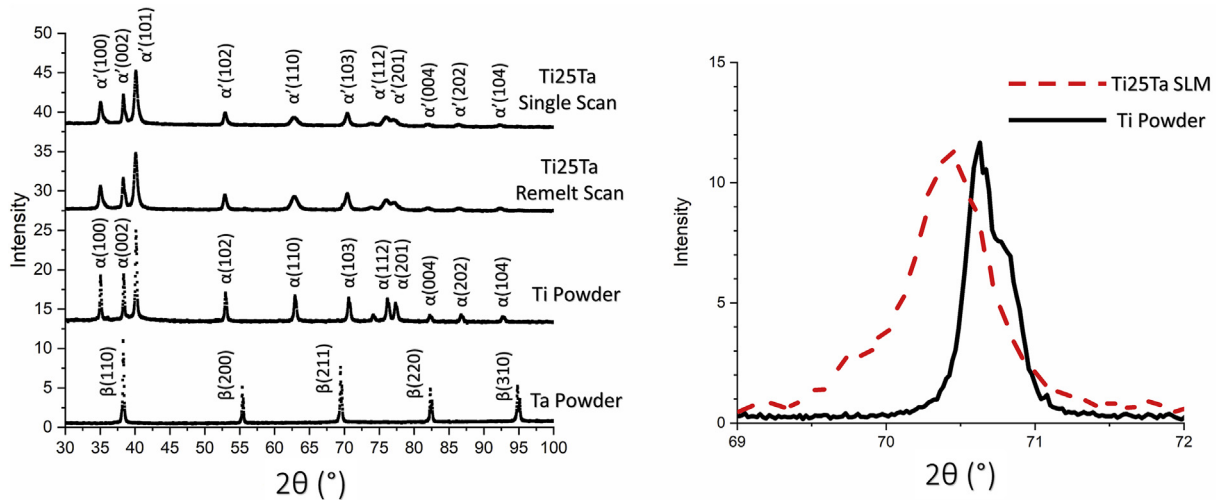


**Fig. 7.** (a) XRD pattern of Ti powder, Ta powder and SLM Ti25Ta for both single and remelt scan conditions (b) Magnification of Ti powder and SLM Ti25Ta overlaid, showing minor shift of patterns and peak broadening, indicating lattice distortion and residual stress.

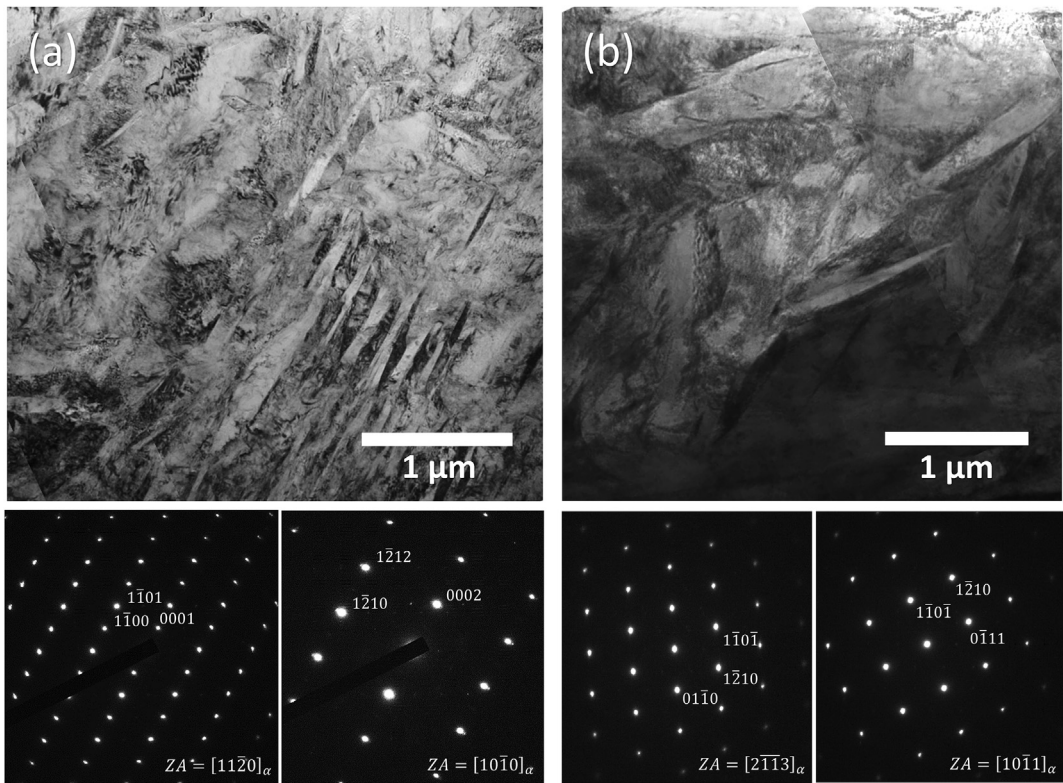


**Fig. 8.** TEM bright field images of microstructure of (a) single scan Ti25Ta and (b) remelt scan Ti25Ta samples in regions with nominal Ta concentration (24–26 wt%). The selected area diffraction patterns indicate only the presence of hexagonal martensite  $\alpha'$ .

in the Ti25Ta single melt (Fig. 8a) and Ti25Ta remelt scan (Fig. 8b) samples. The selected area diffraction patterns from multiple martensitic laths (with two examples shown in Fig. 8 for each of the conditions) failed to identify any phases other than hexagonal  $\alpha'$ , which is consistent with XRD data discussed above. The lattice parameters calculated based on the diffraction patterns are summarised in Table 4.

The structure of a Ta-rich region in the Ti25Ta single melt sample is shown in Fig. 9. A large single grain region on the top right (A) was identified as having a BCC crystal structure with

**Table 4**  
Lattice parameters of phases observed in this study.

Sample	Region	Phase	a, nm	b, nm	c, nm
Ti25Ta Single Melt	nominal	$\alpha'$ (P6 <sub>3</sub> /mmc)	0.2911	—	0.4605
	Ta-rich	$\beta$ (Im3m)	0.3283	—	—
Ti25Ta Remelt	nominal	$\alpha'$ (P6 <sub>3</sub> /mmc)	0.2906	—	0.4602
	Ta-rich	$\alpha'$ (P6 <sub>3</sub> /mmc)	0.2938	—	0.4612
Ti60Ta40 (00-052-0960)	—	$\alpha''$ (Cmcm)	0.2992	0.4917	0.4640
	—	$\alpha''$ (Cmcm)	0.3038	0.4957	0.4686

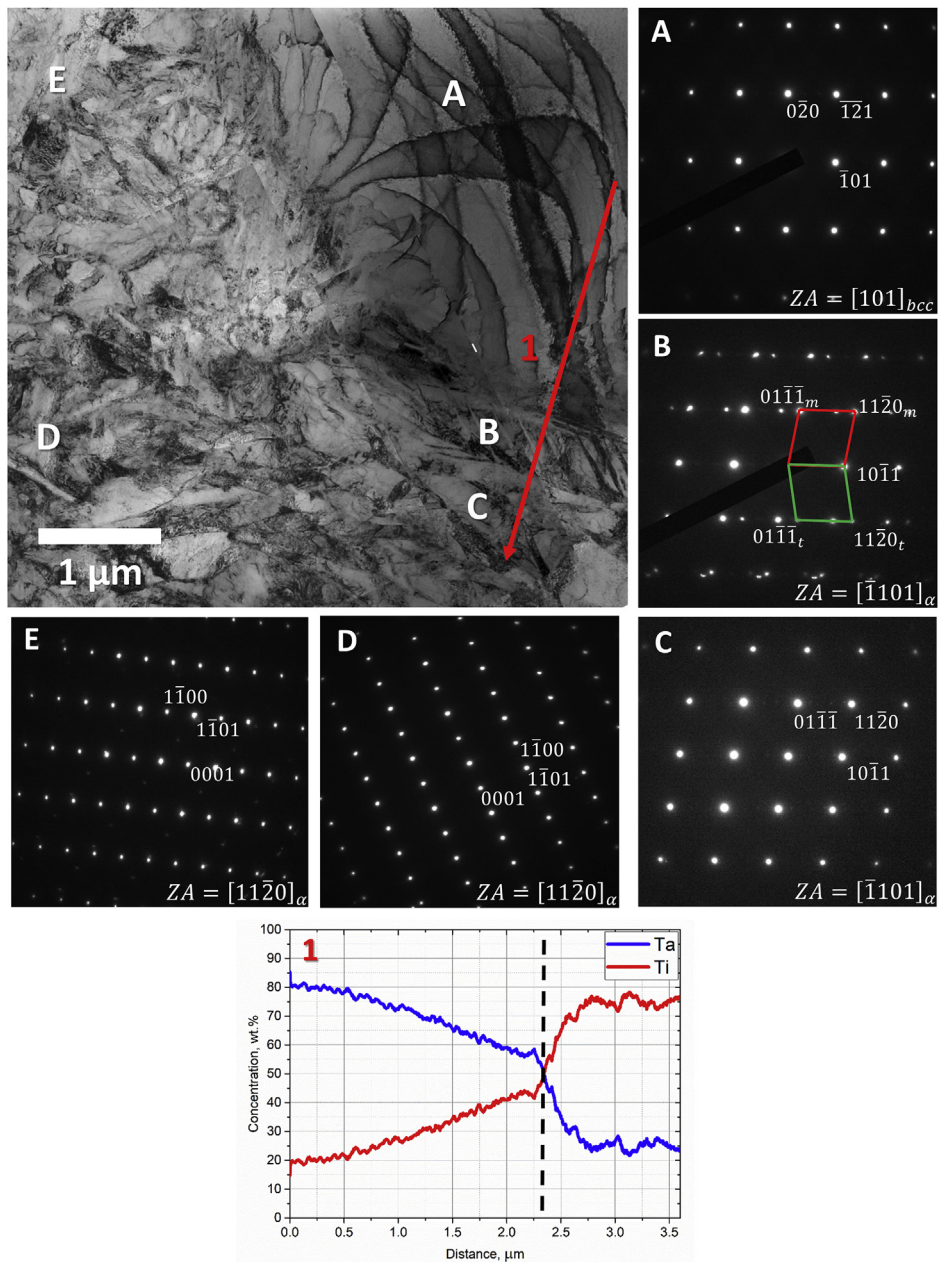


**Fig. 9.** Microstructure of the Ta-rich region within the Ti25Ta single melt sample. A-E show several regions of interest along with the selected area diffraction patterns from these regions. The red arrow indicates the position and direction of the EDX line scan with a respective graph showing the distribution of Ti and Ta along the scan. In the graph, delineation between BCC and  $\alpha'$  phases, as well as between different element concentration regions, is shown as a black dashed line. (For interpretation of the references to colour in this figure legend, the reader is referred to the Web version of this article.)

lattice parameter  $a = 0.3283$  nm as confirmed by SAED (Table 4). The EDX chemical analysis showed that the Ta composition in this region peaked at around 80 wt% with gradual reduction towards the boundary (Fig. 9, line scan 1). This is likely either a region of  $\beta$ -phase that was retained, as the increased Ta content reduced the  $\beta$ -transus temperature, or, more likely, a remnant of a partially melted Ta particle. Pure Ta has a BCC lattice structure (Im3m) which is stable at room temperature with rather significant additions of Ti (as much as 50 wt%) as was shown by Sing et al. [31]. Hence, diffusion of Ti across the boundary would lead to a compositional gradient as seen in the EDX line scan in Fig. 9. Diffusion of Ta into Ti reaches a nominal plateau concentration of around 25 wt%. In the intermediate region with Ta concentrations of 25–50 wt%, the

analysis of several large lamellas (B and C) indicated a lack of orthorhombic  $\alpha''$  martensite. The structure observed has been confirmed as hexagonal, further supported by an observation of  $\{10\bar{1}1\}_{\alpha'}$  twinning (region B). Although this type of twin is not as common as  $\{11\bar{2}1\}_{\alpha}$  or  $\{11\bar{2}2\}_{\alpha}$  [87], it has been observed in samples compressed at elevated temperatures above 400 °C [87–89], and more recently in additively manufactured Ti–6Al–4V [90–92]. An additional study of the structure away from the BCC grain also indicated hexagonal martensite only (regions D and E).

A similar analysis was performed on the Ti25Ta remelt scan samples (Fig. 10). During the analysis, a nano-scale discontinuity was observed in the middle of the specimen (white dashed line, see also the inset), which happened to divide two regions with

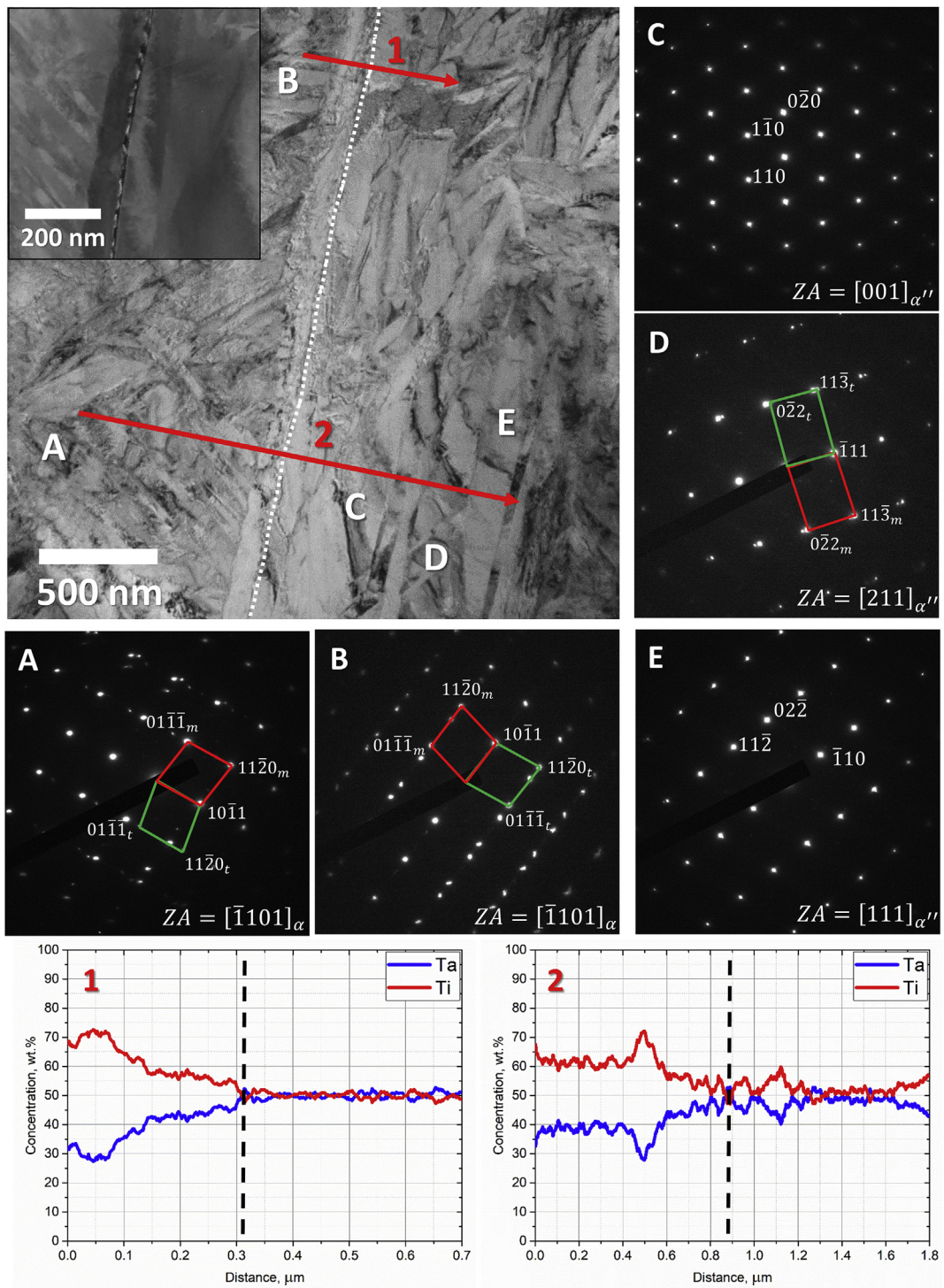


**Fig. 10.** Microstructure of a Ta-rich region of the Ti25Ta remelt scan sample. A-E show several regions of interest along with the selected area diffraction patterns from these regions. The red arrows indicate the position and direction of the EDX line scans with respective graphs showing the distribution of Ti and Ta along the scan. In the graph, delineation between  $\alpha'$  and  $\alpha''$  phases, as well as between different element concentration regions, is shown as a black dashed line. (For interpretation of the references to colour in this figure legend, the reader is referred to the Web version of this article.)

different element concentrations. EDX line scans 1 and 2 indicate that to the left of the discontinuity, the concentration of Ta is around 60–70%, while to the right, the concentration of Ta falls to 50%. Two distinct phases were observed either side of this line; hexagonal (regions A and B) and orthorhombic (Regions C, D and E). Due to the fine size of the hexagonal martensite in the Ti-rich

region, only twinned lamella could be analysed. Twinning has been determined to be a  $\{10\bar{1}1\}_{\alpha'}$  type, similar to the single melt sample. Coarser martensite in the 50%Ta region allowed analysis of three separate laths. Laths C and E were not twinned and were determined to have the orthorhombic structure ( $a = 0.2992$  nm,  $b = 0.4917$  nm,  $c = 0.4640$  nm) consistent with data from PDF card

number 00-052-0960 (Table 4). Lath D had the same structure while also exhibiting  $\{111\}_{\alpha''}$  type I twinning, consistent with previous reports on orthorhombic  $\alpha''$  martensite in Ti–Nb [93] and Ti–Mo [94] alloys.

The major conclusion stemming from the above analysis is that, since orthorhombic martensite is not observed in regions with nominal concentrations of Ta, the  $\alpha'-\alpha''$  transition threshold is believed to lie above 25 wt%. It can also be seen that  $\alpha''$  martensite forms in areas with Ta concentrations close to 50 wt% or slightly below. This finding, however, somewhat disagrees with literature which observes  $\alpha''$  in conventionally manufactured Ti25 wt%Ta alloys [28]. The reason for such inconsistency is unclear at this point and requires further investigation.

Overall, microstructural analysis seems to highlight the role of the remelt scan strategy on the presence of orthorhombic martensite. The remelt seems to facilitate further homogenisation of the structure through enhanced interdiffusion of Ti and Ta in the vicinity of partially melted Ta particles, which leads to extended regions with favourable Ta chemical composition for the formation of orthorhombic  $\alpha''$  martensite.

Nevertheless, the size and quantity of such regions are expected to be very small and exceedingly rare, in particular, given that the amount of partially melted particles was notably reduced after the remelt. This could be the reason for the lack of XRD detection of the  $\alpha''$  phase reported above. Overall, it can be concluded that the SLM Ti25Ta alloy is composed of a single hexagonal martensitic  $\alpha'$  phase with occasional BCC Ta particles.

Following up on these conclusions, we have studied the crystallographic texture evolution in the single and remelt conditions to elucidate the effect of processing conditions on the development of the meso-scale microstructure. Consistent with our discussion above, we have excluded orthorhombic martensite from the analysis due to its negligible volume fraction.

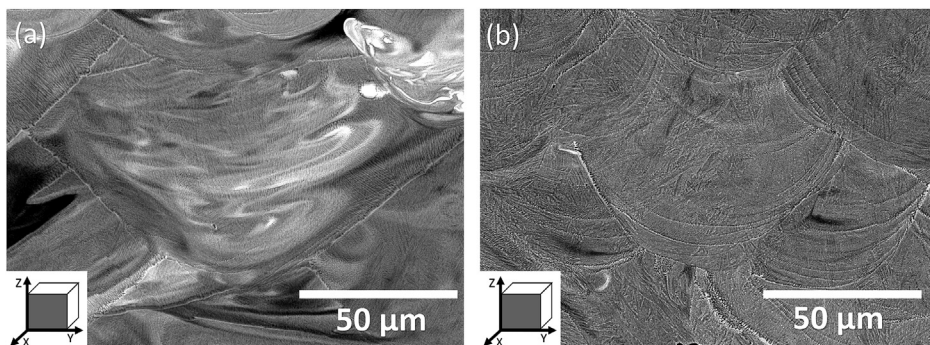
Fig. 11 shows a backscattered electron image of the overlapping melt pool structure of single (Fig. 11a) and remelt scan (Fig. 11b) samples and highlights the difference in homogeneity between the scanning strategies. Multiple contrast regions are observed in the single scan melt pool (Fig. 11a) indicating the mass flow within the melt pool before solidification. This flow, known as 'Marangoni flow', is driven by temperature gradients within the melt pool and is often attributed to the laser beam intensity distribution [95].

The different melt pool size and shape give an indication to the different thermodynamic conditions in each scanning strategy. The melt pool in Fig. 11a has a larger width to height ratio than the melt pool in Fig. 11b. A wider melt pool is indicative of a higher energy density [96], suggesting that during the remelt scan, a lower energy is absorbed. Nevertheless, this smaller melt pool proves sufficient to further melt the partially melted particles in the matrix, likely

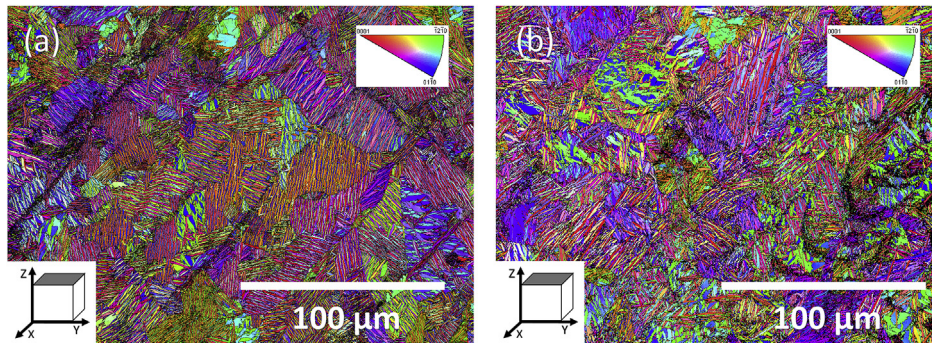
due to their smaller size and the Ti–Ta matrix possessing a much reduced melting temperature compared with pure Ta. The different melt pool shape and thermodynamic conditions experienced during the remelt scan are likely caused by the morphology of the absorbing surface. In the single melt scanning strategy, the laser energy is absorbed by a layer of spherical powder particles, whilst for the remelt scan, the laser energy is absorbed by a flat surface. Simulations have shown that due to multiple scattering of the laser beam between spherical powder particles, a powder layer can absorb up to twice as much laser energy than a flat surface in Ti-based materials [68]. Since the different laser absorption leads to different thermodynamic conditions, it would be expected that the microstructure formation will also differ. In order to clarify this assumption, we performed EBSD analysis to analyse the grain morphology.

Fig. 12a and b shows EBSD inverse pole figure maps of the fine martensitic structure of the single and remelt scan samples, respectively, in the x-y plane, with martensitic laths averaging  $6 \pm 4 \mu\text{m}$  in length and  $0.5 \pm 0.3 \mu\text{m}$  in width. There was no statistical difference in lath size between the single scan and remelt scan samples. The single scan sample (Fig. 12a) shows distinct regions of aligned martensite corresponding to prior  $\beta$  grains, formed as a result of solidification of Ti alloys through a  $\beta$  to  $\alpha'$  pathway, with a crystal directionality link between the martensite and prior  $\beta$  grains [81,97]. The laser scan tracks are also visible, approximately 35  $\mu\text{m}$  wide running at  $45^\circ$  to the horizontal. The remelt scan appears to disrupt the prior  $\beta$  grain structure (Fig. 12b) and the martensite laths become randomly oriented individual plates. This less-aligned martensitic microstructure supports the higher mechanical strength and reduced elongation observed during tensile testing. This latter martensitic microstructure would increase strength and reduce elongation due to randomly oriented crystals providing a more tortuous slip path required for deformation to occur.

The less-aligned martensite morphology shown in Fig. 12b may be caused by a combination of mechanisms. It is hypothesised that a more homogeneous distribution of Ta atoms causes individual lath formation. It is known from literature that substitutional atom additions in the Ti lattice cause a decrease in martensite colony size, which degenerate into randomly oriented individual plates [81]. Furthermore, the thermodynamic conditions experienced during melting and solidification are different between the single melt and remelt conditions, supported by the different melt pool shape and size in Fig. 11. A lower input energy, due to reduced absorption of the laser by the solidified surface, leads to a shallower melt pool [48,96], and, hence, a finer, equiaxed prior  $\beta$  microstructure. In addition, an increased cooling rate, leaving less time for  $\beta$  grain formation and growth, could be a result of the shallower melt pool



**Fig. 11.** Back scattered images showing the melt pool in (a) single scan and (b) remelt scan Ti25Ta. The homogeneity of the melt pool is significantly improved by the remelt scan, however the width to height ratio of the melt pool decreases.



**Fig. 12.** IPF maps of  $\alpha'$  martensite in x-y plane of (a) single and (b) remelt scan sample. The prior  $\beta$  grain structure and martensite alignment, visible in the single melt sample, are disrupted by the remelt scan strategy.

or faster heat transfer from the melt pool when a powder layer is not adjacent to the scan track [52].

IPF maps of the microstructure of the single scan and remelt scan samples in the y-z plane (Fig. 13), covering approximately ten powder layers, show no distinct columnar grains in the building direction, which are commonly seen in additively manufactured titanium [86]. This finding was also confirmed on etched sample surfaces using SEM imaging (Supplementary Fig. 2). The prior  $\beta$  grains observed in (Fig. 13a) are close to equiaxed and measured approximately 10–50  $\mu\text{m}$  in size, however, a slight texture in the  $\alpha'$  martensite is observed in the pole figures. After the remelt scan, prior  $\beta$  grains are no longer easily distinguishable and the  $\alpha'$  martensite texture is notably reduced (Fig. 13b). The second nucleation step, as a result of the remelt scan strategy, appears to reduce structural anisotropy and could potentially be used to reduce anisotropy of mechanical properties across multiple alloy

classes.

The presence of columnar grains in additively manufactured Ti alloys has been attributed to the balance between the temperature gradient ( $G$ ) and the solidification rate ( $R$ ) [86]. A high  $G/R$  ratio results in epitaxial growth and columnar grains. The solidification front, beginning from the pre-solidified layers, is faster than nucleation within the liquid, due to the high thermal gradient between the molten melt pool and cold build plate. A columnar microstructure leads to anisotropic mechanical properties and should be avoided. Strategies to combat epitaxial grain growth include altering the solidification rate through alloy composition, as well as inclusion of known grain refiners such as boron [98].

Compared with pure titanium, the Ti25Ta alloy has an increased solidification rate, and a lower  $G/R$  ratio, resulting in equiaxed grain morphology. This is likely due to local variations in temperature

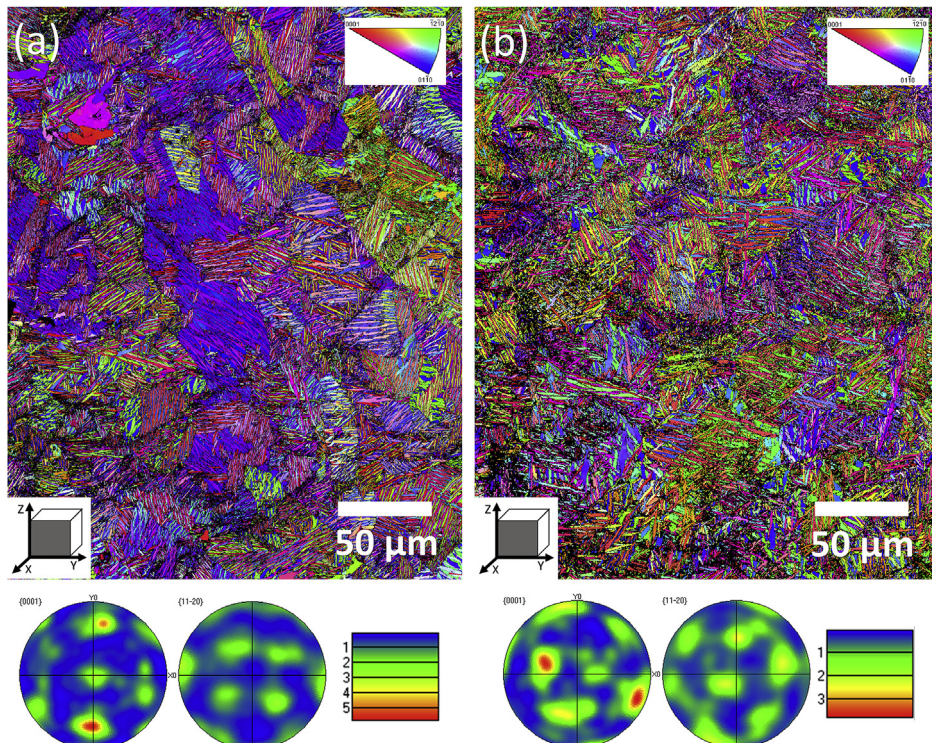


**Fig. 13.** IPF maps of  $\alpha'$  martensite in y-z plane for (a) single scan and (b) remelt scan, showing equiaxed as opposed to columnar grains in the build direction. The slight texture observed in the  $\alpha'$  martensite in the single scan sample is reduced by the remelt scan strategy.

and composition which lead to liquid/solid interface instabilities [98]. The formation of the Ta rich solid phase from the liquid results in constitutional supercooling which allows nucleation ahead of the thermal gradient solidification front and hence promotes equiaxed grain growth. A similar effect was seen in the SLM processing of the Ti50Ta composition where equiaxed grains were attributed to temperature and chemical potential gradients within the melt pool [31]. Compared with the Ti50Ta composition, the temperature range of the liquid +  $\beta$  phase zone is smaller (36°–91° respectively), suggesting a lower resistance to epitaxial growth. However, the constitutional undercooling in the Ti25Ta composition still proves enough to disrupt epitaxial growth in SLM processing, likely due to the slow diffusion rate of Ta.

In addition, the remaining partially melted Ta particles likely act as heterogeneous sites for  $\beta$  crystal growth. Tedman-Jones et al. [99] showed partially melted refractory particles such as W and Nb at the centre of dendrites in wire arc melted Ti alloys. It is hypothesised that the partial dissolution of the particle causes an enrichment of the liquid around the particle, raising the equilibrium liquid temperature and facilitating crystal growth on these particles. This was termed 'dissolutional supercooling' and is likely contributing to the equiaxed grain structure noted in this study.

Overall, it can be concluded that the remelt scan strategy improves the chemical homogeneity of the material, increases the material strength without increasing the elastic modulus and reduces grain texture and microstructure anisotropy. However, the disordered microstructure results in a lower elongation and could influence the fatigue performance of the Ti25Ta alloy, which is critical for implants loaded in a cyclic manner. Further studies investigating the fatigue performance of single and remelt scan samples are underway and will be reported elsewhere.

#### 4. Conclusions

In this work the feasibility of SLM processing of Ti25Ta was investigated through parameter optimisation and the application of a remelt scan strategy. The resulting mechanical properties and microstructure were assessed and the main conclusions are as follows;

- 1) Fully dense Ti25Ta (>99.9%) was produced from mixed powders through SLM processing. Adjusting the volumetric energy density through the variation of scanning speed was insufficient to produce homogeneous Ti25Ta compositions, as low speeds required to fully melt the refractory tantalum caused keyhole formation in the titanium. The application of a remelt scanning strategy led to dense and chemically homogeneous material.
- 2) SLM Ti25Ta retained similar strength, elongation and elastic modulus to conventionally wrought Ti25Ta and possessed a superior strength to modulus ratio to SLM CP Ti. The remelt scan strategy caused a 50 MPa increase in strength but reduced the elongation by half.
- 3) The SLM Ti25Ta predominantly consisted of hexagonal  $\alpha'$  martensite within equiaxed prior  $\beta$  grains. However, local Ta-rich regions in the vicinity of partially melted Ta particles exhibited a limited amount of orthorhombic  $\alpha''$  martensite. The composition range for the orthorhombic phase was tentatively observed as 40–50 wt% Ta.
- 4) The remelt scan favoured the formation of  $\alpha''$  phase, due to the formation of regions with high Ta concentrations, as a result of intensified diffusion.

- 5) The remelt scan improved material homogeneity, reduced texture and disrupted the prior  $\beta$  grain structure visible in the single scan sample.

#### Author contributions section

E. G. Brodie: Methodology, Formal analysis, Investigation, Writing - Original Draft, Writing - Review & Editing. A. E. Medvedev: Investigation, Formal analysis, Writing - Original Draft, Writing - Review & Editing. J. E. Frith: Writing - Review & Editing, Supervision. M. S. Dargusch: Writing - Review & Editing, Funding acquisition. H. L. Fraser: Writing - Review & Editing. A. Molotnikov: Conceptualization, Writing - Review & Editing, Supervision, Funding acquisition.

#### Declaration of competing interest

The authors declare that they have no known competing financial interests or personal relationships that could have appeared to influence the work reported in this paper.

#### Acknowledgments

E.G.B. would like to acknowledge the Monash Centre for Electron Microscopy and the Monash X-ray Platform. A.E.M. acknowledges the use of facilities within the RMIT Microscopy and Microanalysis Facility (RMMF). This project is funded by the ARC Research Hub for Transforming Australia's Manufacturing Industry through High Value Additive Manufacturing (IH130100008). M.S.D. would also like to acknowledge the support of the ARC Research Hub for Advanced Manufacturing of Medical Devices (IH150100024). A.M. would also like to acknowledge the support of the Garnett Passe and Rodney Williams Memorial Foundation 2019 Conjoint Grant.

#### Appendix A. Supplementary data

Supplementary data to this article can be found online at <https://doi.org/10.1016/j.jallcom.2019.153082>.

#### References

- [1] M. Touri, F. Kabirian, M. Saadati, S. Ramakrishna, M. Mozafari, Additive manufacturing of biomaterials – the evolution of rapid prototyping, *Adv. Eng. Mater.* 21 (2019) 1800511.
- [2] M. Kaur, K. Singh, Review on titanium and titanium based alloys as biomaterials for orthopaedic applications, *Mater. Sci. Eng. C* 102 (2019) 844–862.
- [3] X. Feng, G. Lin, C.X. Fang, W.W. Lu, B. Chen, F.K.L. Leung, Bone resorption triggered by high radial stress: the mechanism of screw loosening in plate fixation of long bone fractures, *J. Orthop. Res.* 37 (2019) 1498–1507.
- [4] M. Niinomi, Design and development of metallic biomaterials with biological and mechanical biocompatibility, *J. Biomed. Mater. Res. A* 107 (2019) 944–954.
- [5] D. Zhang, C.S. Wong, C. Wen, Y. Li, Cellular responses of osteoblast-like cells to 17 elemental metals, *J. Biomed. Mater. Res. A* 105 (2017) 148–158.
- [6] C. Exley, M.J. Mold, Aluminium in human brain tissue: how much is too much? *J. Biol. Inorg. Chem.* (2019) <https://doi.org/10.1007/s00775-019-01710-0>.
- [7] Y.L. Zhou, M. Niinomi, T. Akahori, Effects of Ta content on Young's modulus and tensile properties of binary Ti-Ta alloys for biomedical applications, *Mater. Sci. Eng. A* 371 (2004) 283–290.
- [8] Y. Liu, S. Xu, X. Wang, K. Li, B. Liu, H. Wu, H. Tang, Ultra-high strength and ductile lamellar-structured powder metallurgy binary Ti-Ta alloys, *JOM* 68 (2016) 899–907.
- [9] H.J. Maier, E. Karsten, A. Paulsen, D. Langenkämper, P. Decker, J. Frenzel, C. Somsen, A. Ludwig, G. Eggerer, T. Niendorf, Microstructural evolution and functional fatigue of a Ti–25Ta high-temperature shape memory alloy, *J. Mater. Res.* 32 (2017) 4287–4295.
- [10] C.-M. Wu, P.-W. Peng, H.-H. Chou, K.-L. Ou, E. Sugiatno, C.-M. Liu, C.-F. Huang, Microstructural, mechanical and biological characterizations of the promising titanium-tantalum alloy for biomedical applications, *J. Alloy. Comp.* 735

- (2018) 2604–2610.
- [11] G. Chen, J. Yin, S. Zhao, H. Tang, X. Qu, Microstructure and tensile properties of a Ti-28Ta alloy studied by transmission electron microscopy and digital image correlation, *Int. J. Refract. Metals Hard Mater.* 81 (2019) 71–77.
- [12] L. Zhou, T. Yuan, R. Li, J. Tang, M. Wang, L. Li, C. Chen, Microstructure and mechanical performance tailoring of Ti-13Nb-13Zr alloy fabricated by selective laser melting after post heat treatment, *J. Alloy. Comp.* 775 (2019) 1164–1176.
- [13] Y. Li, Y. Ding, K. Munir, J. Lin, M. Brandt, A. Atrens, Y. Xiao, J.R. Kanwar, C. Wen, Novel  $\beta$ -Ti35Zr28Nb alloy scaffolds manufactured using selective laser melting for bone implant applications, *Acta Biomater.* (2019) 273–284.
- [14] L.C. Zhang, T.B. Sercombe, Selective laser melting of low-modulus biomedical Ti-24Nb-4Zr-8Sn alloy: effect of laser point distance, *Key Eng. Mater.* 520 (2012) 226–233.
- [15] C.L. Yang, Z.J. Zhang, S.J. Li, Y.J. Liu, T.B. Sercombe, W.T. Hou, P. Zhang, Y.K. Zhu, Y.L. Hao, Z.F. Zhang, R. Yang, Simultaneous improvement in strength and plasticity of Ti-24Nb-4Zr-8Sn manufactured by selective laser melting, *Mater. Des.* 157 (2018) 52–59.
- [16] Y.J. Liu, S.J. Li, H.L. Wang, W.T. Hou, Y.L. Hao, R. Yang, T.B. Sercombe, L.C. Zhang, Microstructure, defects and mechanical behavior of beta-type titanium porous structures manufactured by electron beam melting and selective laser melting, *Acta Mater.* 113 (2016) 56–67.
- [17] M. Fischer, D. Joguet, G. Robin, L. Peltier, P. Laheurte, In situ elaboration of a binary Ti-26Nb alloy by selective laser melting of elemental titanium and niobium mixed powders, *Mater. Sci. Eng. C* 62 (2016) 852–859.
- [18] M. Weinmann, C. Schnitter, M. Stenzel, J. Markhoff, C. Schulze, R. Bader, Development of bio-compatible refractory Ti/Nb/Ta alloys for application in patient-specific orthopaedic implants, *Int. J. Refract. Metals Hard Mater.* 75 (2018) 126–136.
- [19] J. Wei, H. Sun, D. Zhang, L. Gong, J. Lin, C. Wen, Influence of heat treatments on microstructure and mechanical properties of Ti-26Nb alloy elaborated in situ by laser additive manufacturing with Ti and Nb mixed powder, *Materials* 12 (2018) 61.
- [20] C. Schulze, M. Weinmann, C. Schweigel, O. Keßler, R. Bader, Mechanical properties of a newly additive manufactured implant material based on Ti-42Nb, *Materials* 11 (2018) 124.
- [21] Y. Guo, J. Wu, K. Xie, J. Tan, Y. Yang, S. Zhao, L. Wang, W. Jiang, Y. Hao, Study of bone regeneration and osseointegration effect of a novel selective laser melted titanium-tantalum-niobium-zirconium alloy scaffold, *ACS Biomater. Sci. Eng.* (2019), <https://doi.org/10.1021/acsbiomaterials.9b00909>.
- [22] A. Bandyopadhyay, I. Mitra, A. Shivaram, N. Dasgupta, S. Bose, Direct comparison of additively manufactured porous titanium and tantalum implants towards *in vivo* osseointegration, *Addit. Manuf.* 28 (2019) 259–266.
- [23] M. Stiehler, M. Lind, T. Mygind, A. Baatrup, A. Dolatshahi-Pirouz, H. Li, M. Foss, F. Besenbacher, M. Kassem, C. Bünger, Morphology, proliferation, and osteogenic differentiation of mesenchymal stem cells cultured on titanium, tantalum, and chromium surfaces, *J. Biomed. Mater. Res. A* 86A (2008) 448–458.
- [24] Y. Zhu, Y. Gu, S. Qiao, L. Zhou, J. Shi, H. Lai, Bacterial and mammalian cells adhesion to tantalum-decorated micro-/nano-structured titanium, *J. Biomed. Mater. Res. A* 105 (2017) 871–878.
- [25] V.K. Balla, S. Banerjee, S. Bose, A. Bandyopadhyay, Direct laser processing of a tantalum coating on titanium for bone replacement structures, *Acta Biomater.* 6 (2010) 2329–2334.
- [26] R. Wauthle, J. van der Stok, S. Amin Yavari, J. Van Humbeeck, J.-P. Kruth, A.A. Zadpoor, H. Weinans, M. Mulier, J. Schrooten, Additively manufactured porous tantalum implants, *Acta Biomater.* 14 (2015) 217–225.
- [27] J. Tae-Sik, J. Hyun-Do, K. Sungwon, M. Byeong-Seok, B. Jaeuk, P. Cheonil, S. Juha, K. Hyoun-Ee, Multiscale porous titanium surfaces via a two-step etching process for improved mechanical and biological performance, *Bio-med. Mater.* 12 (2017), 025008.
- [28] Y.-L. Zhou, M. Niinomi, Ti-25Ta alloy with the best mechanical compatibility in Ti-Ta alloys for biomedical applications, *Mater. Sci. Eng. C* 29 (2009) 1061–1065.
- [29] L. Zhou, T. Yuan, R. Li, J. Tang, G. Wang, K. Guo, Selective laser melting of pure tantalum: densification, microstructure and mechanical behaviors, *Mater. Sci. Eng. A* 707 (2017) 443–451.
- [30] V. Livescu, C.M. Knapp, G.T. Gray, R.M. Martinez, B.M. Morrow, B.G. Ndefru, Additively manufactured tantalum microstructures, *Materialia* 1 (2018) 15–24.
- [31] S.L. Sing, W.Y. Yeong, F.E. Wiria, Selective laser melting of titanium alloy with 50 wt% tantalum: microstructure and mechanical properties, *J. Alloy. Comp.* 660 (2016) 461–470.
- [32] S.L. Sing, F.E. Wiria, W.Y. Yeong, Selective laser melting of titanium alloy with 50 wt% tantalum: effect of laser process parameters on part quality, *Int. J. Refract. Metals Hard Mater.* 77 (2018) 120–127.
- [33] D. Zhao, C. Han, Y. Li, J. Li, K. Zhou, Q. Wei, J. Liu, Y. Shi, Improvement on mechanical properties and corrosion resistance of titanium-tantalum alloys in-situ fabricated via selective laser melting, *J. Alloy. Comp.* 804 (2019) 288–298.
- [34] L.C. Zhang, D. Klemm, J. Eckert, Y.L. Hao, T.B. Sercombe, Manufacture by selective laser melting and mechanical behavior of a biomedical Ti-24Nb-4Zr-8Sn alloy, *Scr. Mater.* 65 (2011) 21–24.
- [35] Z. Wang, Z. Xiao, Y. Tse, C. Huang, W. Zhang, Optimization of processing parameters and establishment of a relationship between microstructure and mechanical properties of SLM titanium alloy, *Opt. Laser. Technol.* 112 (2019) 159–167.
- [36] T. DebRoy, H.L. Wei, J.S. Zuback, T. Mukherjee, J.W. Elmer, J.O. Milewski, A.M. Beese, A. Wilson-Heid, A. De, W. Zhang, Additive manufacturing of metallic components – process, structure and properties, *Prog. Mater. Sci.* 92 (2018) 112–224.
- [37] S.M. Yusuf, N. Gao, Influence of energy density on metallurgy and properties in metal additive manufacturing, *Mater. Sci. Technol.* (2017) 1–21.
- [38] K.G. Prashanth, S. Scudino, T. Maity, J. Das, J. Eckert, Is the energy density a reliable parameter for materials synthesis by selective laser melting? *Mater. Res. Lett.* 5 (2017) 386–390.
- [39] S. Ghose, S. Babu, R.J. Van Arkel, K. Nai, P.A. Hooper, J.R.T. Jeffers, The influence of laser parameters and scanning strategies on the mechanical properties of a stochastic porous material, *Mater. Des.* 131 (2017) 498–508.
- [40] W.E. King, H.D. Barth, V.M. Castillo, G.F. Gallegos, J.W. Gibbs, D.E. Hahn, C. Kamath, A.M. Rubenchik, Observation of keyhole-mode laser melting in laser powder-bed fusion additive manufacturing, *J. Mater. Process. Technol.* 214 (2014) 2915–2925.
- [41] C.A. Biffi, A.G. Demir, M. Coduri, B. Previtali, A. Tuissi, Laves phases in selective laser melted TiCr1.78 alloys for hydrogen storage, *Mater. Lett.* 226 (2018) 71–74.
- [42] R. Martinez, I. Todd, K. Mumtaz, In situ alloying of elemental Al-Cu12 feedstock using selective laser melting, *Virtual Phys. Prototyp.* 14 (2019) 242–252.
- [43] J.C. Wang, Y.J. Liu, P. Qin, S.X. Liang, T.B. Sercombe, L.C. Zhang, Selective laser melting of Ti-35Nb composite from elemental powder mixture: microstructure, mechanical behavior and corrosion behavior, *Mater. Sci. Eng. A* 760 (2019) 214–224.
- [44] K. Majchrowicz, Z. Pakiela, T. Brynk, B. Romelczyk-Baishya, M. Płocińska, T. Kurzynowski, E. Chlebus, Microstructure and mechanical properties of Ti-Re alloys manufactured by selective laser melting, *Mater. Sci. Eng., A* 765 (2019) 138290.
- [45] Y. Guo, L. Jia, B. Kong, N. Wang, H. Zhang, Single track and single layer formation in selective laser melting of niobium solid solution alloy, *Chin. J. Aeronaut.* 31 (2018) 860–866.
- [46] P.F. Zhou, D.H. Xiao, Z. Wu, X.Q. Ou, Al0.5FeCoCrNi high entropy alloy prepared by selective laser melting with gas-atomized pre-alloy powders, *Mater. Sci. Eng., A* 739 (2019) 86–89.
- [47] A. Ilevković, N. Omidivari, B. Vrancken, K. Lietaert, L. Thijs, K. Vanmeensel, J. Vleugels, J.-P. Kruth, Selective laser melting of tungsten and tungsten alloys, *Int. J. Refract. Metals Hard Mater.* 72 (2018) 27–32.
- [48] B. Liu, B.-Q. Li, Z. Li, Selective laser remelting of an additive layer manufacturing process on AlSi10Mg, *Results Phys.* 12 (2019) 982–988.
- [49] W. Yu, S.L. Sing, C.K. Chua, X. Tian, Influence of re-melting on surface roughness and porosity of AlSi10Mg parts fabricated by selective laser melting, *J. Alloy. Comp.* 792 (2019) 574–581.
- [50] T. Gustmann, H. Schwab, U. Kühn, S. Pauly, Selective laser remelting of an additively manufactured Cu-Al-Ni-Mn shape-memory alloy, *Mater. Des.* 153 (2018) 129–138.
- [51] A.G. Demir, B. Previtali, Investigation of remelting and preheating in SLM of 18Ni300 maraging steel as corrective and preventive measures for porosity reduction, *Int. J. Adv. Manuf. Technol.* 93 (2017) 2697–2709.
- [52] B. AlMangour, D. Grzesiak, J.-M. Yang, Scanning strategies for texture and anisotropy tailoring during selective laser melting of TiC/316L stainless steel nanocomposites, *J. Alloy. Comp.* 728 (2017) 424–435.
- [53] B. Richter, N. Blanke, C. Werner, N.D. Parab, T. Sun, F. Vollertsen, F.E. Pfefferkorn, High-speed X-ray investigation of melt dynamics during continuous-wave laser remelting of selective laser melted Co-Cr alloy, *CIRP Ann.* 68 (2019) 229–232.
- [54] S. Huang, S.L. Sing, W.Y. Yeong, Selective laser melting of Ti42Nb composite powder and the effect of laser Re-melting, *Key Eng. Mater.* 801 (2019) 270–275.
- [55] S. Itoh, S. Shukla (Eds.), *Advanced Surface Enhancement*, Springer Singapore, Singapore, 2020.
- [56] X. Yang, J. Liu, X. Cui, G. Jin, Z. Liu, Y. Chen, X. Feng, Effect of remelting on microstructure and magnetic properties of Fe-Co-based alloys produced by laser additive manufacturing, *J. Phys. Chem. Solids* 130 (2019) 210–216.
- [57] P. Majumdar, S.B. Singh, M. Chakraborty, Elastic modulus of biomedical titanium alloys by nano-indentation and ultrasonic techniques—a comparative study, *Mater. Sci. Eng., A* 489 (2008) 419–425.
- [58] B. Chalmers, *The Physical Examination of Metals*, second ed., Edward Arnold, London, 1960.
- [59] R. Cunningham, S.P. Narra, C. Montgomery, J. Beuth, A.D. Rollett, Synchrotron-based X-ray microtomography characterization of the effect of processing variables on porosity formation in laser power-bed additive manufacturing of Ti-6Al-4V, *JOM* 69 (2017) 479–484.
- [60] M. Geiger, K.H. Leitz, H. Koch, A. Otto, A 3D transient model of keyhole and melt pool dynamics in laser beam welding applied to the joining of zinc coated sheets, *Prod. Eng.* 3 (2009) 127–136.
- [61] R. Cunningham, C. Zhao, N. Parab, C. Kantzios, J. Pauza, K. Fezzaa, T. Sun, A.D. Rollett, Keyhole threshold and morphology in laser melting revealed by ultrahigh-speed x-ray imaging, *Science* 363 (2019) 849.
- [62] H. Attar, M. Calin, L.C. Zhang, S. Scudino, J. Eckert, Manufacture by selective laser melting and mechanical behavior of commercially pure titanium, *Mater. Sci. Eng., A* 593 (2014) 170–177.
- [63] Q. Guo, C. Zhao, L.I. Escano, Z. Young, L. Xiong, K. Fezzaa, W. Everhart,

- B. Brown, T. Sun, L. Chen, Transient dynamics of powder spattering in laser powder bed fusion additive manufacturing process revealed by in-situ high-speed high-energy x-ray imaging, *Acta Mater.* 151 (2018) 169–180.
- [64] C.L.A. Leung, S. Marussi, R.C. Atwood, M. Towrie, P.J. Withers, P.D. Lee, In situ X-ray imaging of defect and molten pool dynamics in laser additive manufacturing, *Nat. Commun.* 9 (2018) 1355.
- [65] C.L.A. Leung, S. Marussi, M. Towrie, R.C. Atwood, P.J. Withers, P.D. Lee, The effect of powder oxidation on defect formation in laser additive manufacturing, *Acta Mater.* 166 (2019) 294–305.
- [66] C.L.A. Leung, S. Marussi, M. Towrie, J. del Val Garcia, R.C. Atwood, A.J. Bodey, J.R. Jones, P.J. Withers, P.D. Lee, Laser-matter interactions in additive manufacturing of stainless steel SS316L and 13-93 bioactive glass revealed by in situ X-ray imaging, *Addit. Manuf.* 24 (2018) 647–657.
- [67] N.K. Tolochko, Y.V. Khlopkov, S.E. Mozzharov, M.B. Ignatiev, T. Laoui, V.I. Titov, Absorptance of powder materials suitable for laser sintering, *Rapid Prototyp. J.* 6 (2000) 155–160.
- [68] W.E. King, A.T. Anderson, R.M. Ferencz, N.E. Hodge, C. Kamath, S.A. Khairallah, A.M. Rubenchik, Laser powder bed fusion additive manufacturing of metals; physics, computational, and materials challenges, *Appl. Phys. Rev.* 2 (2015), 041304.
- [69] E.D. Palik, *Handbook of Optical Constants of Solids*, Academic Press, Orlando, 1985.
- [70] M.A. Ordal, R.J. Bell, R.W. Alexander, L.A. Newquist, M.R. Querry, Optical properties of Al, Fe, Ti, Ta, W, and Mo at submillimeter wavelengths, *Appl. Opt.* 27 (1988) 1203–1209.
- [71] R. Rai, J.W. Elmer, T.A. Palmer, T. DebRoy, Heat transfer and fluid flow during keyhole mode laser welding of tantalum, Ti–6Al–4V, 304L stainless steel and vanadium, *J. Phys. D Appl. Phys.* 40 (2007) 5753–5766.
- [72] CES EduPack, Granta Design Limited, 2019.
- [73] K. Zhou, H.P. Wang, J. Chang, B. Wei, Experimental study of surface tension, specific heat and thermal diffusivity of liquid and solid titanium, *Chem. Phys. Lett.* 639 (2015) 105–108.
- [74] G. Pottlacher, A. Seifter, Microsecond laser polarimetry for emissivity measurements on liquid metals at high temperatures—application to tantalum, *Int. J. Thermophys.* 23 (2002) 1281–1291.
- [75] O.N. Senkov, J.J. Jonas, Dynamic strain aging and hydrogen-induced softening in alpha titanium, *Metall. Mater. Trans. A* 27 (1996) 1877–1887.
- [76] I. Weiss, S.L. Semiatin, Thermomechanical processing of alpha titanium alloys—an overview, *Mater. Sci. Eng., A* 263 (1999) 243–256.
- [77] Z. Zeng, Y. Zhang, S. Jonsson, Deformation behaviour of commercially pure titanium during simple hot compression, *Mater. Des.* 30 (2009) 3105–3111.
- [78] N. Srinivasan, R. Velmurugan, R. Kumar, S.K. Singh, B. Pant, Deformation behavior of commercially pure (CP) titanium under equi-biaxial tension, *Mater. Sci. Eng., A* 674 (2016) 540–551.
- [79] R. Wauthle, S.M. Ahmadi, S. Amin Yavari, M. Mulier, A.A. Zadpoor, H. Weinans, J. Van Humbeeck, J.-P. Kruth, J. Schrooten, Revival of pure titanium for dynamically loaded porous implants using additive manufacturing, *Mater. Sci. Eng. C* 54 (2015) 94–100.
- [80] D. Herzog, V. Seyda, E. Wycisk, C. Emmelmann, Additive manufacturing of metals, *Acta Mater.* 117 (2016) 371–392.
- [81] I.J. Polmear, D. StJohn, J. Nie, M. Qian (Eds.), *Light Alloys*, Butterworth-Heinemann, Oxford, 2017.
- [82] M. Niinomi, T. Narushima, M. Nakai (Eds.), *Advances in Metallic Biomaterials: Tissues, Materials and Biological Reactions*, Springer Heidelberg, Heidelberg, 2015.
- [83] S.J. Li, Y.W. Zhang, B.B. Sun, Y.L. Hao, R. Yang, Thermal stability and mechanical properties of nanostructured Ti–24Nb–4Zr–7.9Sn alloy, *Mater. Sci. Eng., A* 480 (2008) 101–108.
- [84] S. Ozan, J. Lin, Y. Li, R. Ipek, C. Wen, Development of Ti–Nb–Zr alloys with high elastic admissible strain for temporary orthopedic devices, *Acta Biomater.* 20 (2015) 176–187.
- [85] A.A. Zadpoor, Mechanical performance of additively manufactured meta-biomaterials, *Acta Biomater.* 85 (2019) 41–59.
- [86] P.C. Collins, D.A. Brice, P. Samimi, I. Ghamarian, H.L. Fraser, Microstructural control of additively manufactured metallic materials, *Annu. Rev. Mater. Res.* 46 (2016) 63–91.
- [87] G. Lütjering, J.C. Williams (Eds.), *Titanium*, Springer-Verlag Berlin Heidelberg, 2007.
- [88] Y.J. Li, Y.J. Chen, J.C. Walmsley, R.H. Mathiesen, S. Dumoulin, H.J. Roven, Faceted interfacial structure of {1011} twins in Ti formed during equal channel angular pressing, *Scr. Mater.* 62 (2010) 443–446.
- [89] I. Kim, J. Kim, D. Shin, C.S. Lee, S. Hwang, Effects of equal channel angular pressing temperature on deformation structures of pure Ti, *Mater. Sci. Eng. A-Struct. Mater. Prop. Microstruct. Process.* 342 (2003) 302–310.
- [90] H.Z. Zhong, X.Y. Zhang, S.X. Wang, J.F. Gu, Examination of the twinning activity in additively manufactured Ti-6Al-4V, *Mater. Des.* 144 (2018) 14–24.
- [91] S. Cao, R. Chu, X. Zhou, K. Yang, Q. Jia, C.V.S. Lim, A. Huang, X. Wu, Role of martensite decomposition in tensile properties of selective laser melted Ti-6Al-4V, *J. Alloy. Comp.* 744 (2018) 357–363.
- [92] X. Tan, Y. Kok, Y.J. Tan, M. Descoings, D. Mangelinck, S.B. Tor, K.F. Leong, C.K. Chua, Graded microstructure and mechanical properties of additive manufactured Ti-6Al-4V via electron beam melting, *Acta Mater.* 97 (2015) 1–16.
- [93] Y.W. Chai, H.Y. Kim, H. Hosoda, S. Miyazaki, Interfacial defects in Ti–Nb shape memory alloys, *Acta Mater.* 56 (2008) 3088–3097.
- [94] X. Ji, I. Gutierrez-Urrutia, S. Emura, T. Liu, T. Hara, X. Min, D. Ping, K. Tsuchiya, Twinning behavior of orthorhombic- $\alpha''$  martensite in a Ti-7.5Mo alloy, *Sci. Technol. Adv. Mater.* 20 (2019) 401–411.
- [95] M. Brandt (Ed.), *Laser Additive Manufacturing*, Woodhead Publishing, Kent, 2017.
- [96] A. Bandyopadhyay, S. Bose (Eds.), *Additive Manufacturing*, CRC Press, Boca Raton, 2015.
- [97] M. Simonelli, Y.Y. Tse, C. Tuck, The formation of [alpha] + [beta] microstructure in as-fabricated selective laser melting of Ti-6Al-4V, *J. Mater. Res.* 29 (2014) 2028–2035.
- [98] P. Barriobero-Vila, J. Gussone, A. Stark, N. Schell, J. Haubrich, G. Requena, Peritectic titanium alloys for 3D printing, *Nat. Commun.* 9 (2018) 3426.
- [99] S.N. Tedman-Jones, S.D. McDonald, M.J. Bermingham, D.H. StJohn, M.S. Dargusch, A new approach to nuclei identification and grain refinement in titanium alloys, *J. Alloy. Comp.* 794 (2019) 268–284.